ACS central science

http://pubs.acs.org/journal/acscii

Article

Effect of Framework Composition and NH_3 on the Diffusion of Cu^+ in Cu-CHA Catalysts Predicted by Machine-Learning Accelerated Molecular Dynamics

Reisel Millan, Estefanía Bello-Jurado, Manuel Moliner, Mercedes Boronat,* and Rafael Gomez-Bombarelli*

Cite This: *ACS Cent. Sci.* 2023, 9, 2044−2056

Read Online

ACCESS | Metrics & More | Article Recommendations | Supporting Information

ABSTRACT: Cu-exchanged zeolites rely on mobile solvated Cu^+ cations for their catalytic activity, but the role of the framework composition in transport is not fully understood. Ab initio molecular dynamics simulations can provide quantitative atomistic insight but are too computationally expensive to explore large length and time scales or diverse compositions. We report a machine-learning interatomic potential that accurately reproduces ab initio results and effectively generalizes to allow multinano-second simulations of large supercells and diverse chemical compositions. Biased and unbiased simulations of $[Cu(NH_3)_2]^+$ mobility show that aluminum pairing in eight-membered rings accelerates local hopping and demonstrate that increased NH_3 concentration enhances long-range diffusion. The probability of finding two $[Cu(NH_3)_2]^+$ complexes in the same cage, which is key for SCR-NOx reaction, increases with Cu content and Al content but does not correlate with the long-range mobility of Cu^+. Supporting experimental evidence was obtained from reactivity tests of Cu-CHA catalysts with a controlled chemical composition.

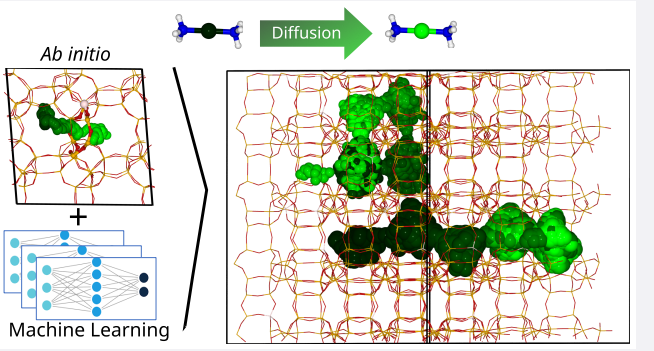

INTRODUCTION

Copper-exchanged zeolites play a crucial role as redox catalysts for some environmentally relevant processes, such as the partial methane oxidation to methanol or the selective catalytic reduction of nitrogen oxides with ammonia (NH_3−SCR−NO_x). In both cases, the small pore Cu-SSZ-13 zeolite with the CHA structure has been reported as an efficient catalyst.[1−11]

The NH_3−SCR−NO_x reaction is currently employed for the removal of nitrogen oxides (NOx) from exhaust gases in diesel vehicles and stationary plants through a redox catalytic cycle in which Cu^+ is oxidized to Cu^{2+} by O_2, NO_2, or NO + O_2 and then reduced to Cu^+ by the reaction of NH_3 and NO forming harmless N_2 + H_2O (Scheme 1).[12−16] This understanding of the reaction mechanism has enabled the development of optimized catalysts by tuning the framework topology, composition, and copper speciation. In the as-prepared catalysts, Cu^+ and Cu^{2+} cations are directly coordinated to the zeolite framework forming heterogeneous active sites, while under reaction conditions NH_3 solvates the Cu^+ cations forming mobile $[Cu(NH_3)_2]^+$ complexes that act as dynamic active sites, resembling homogeneous catalysts but within the confinement of the zeolite pores. At low temperature, that is, between 423 and 523 K, the oxidation step involves transient dimeric $[Cu(NH_3)_2$−OO−$Cu(NH_3)_2]^{2+}$ species whose formation requires the simultaneous presence of two [Cu-

Scheme 1. Illustration of the Low-Temperature SCR-NOx Redox Cycle

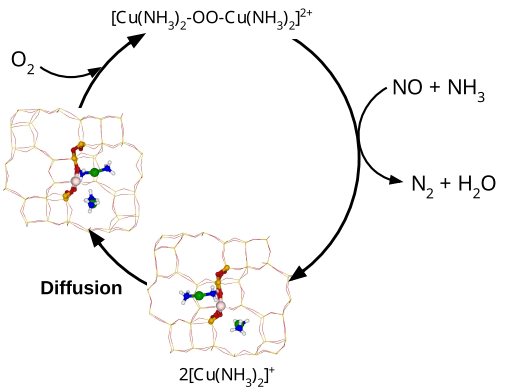

Received: July 13, 2023
Published: October 18, 2023

https://doi.org/10.1021/acscentsci.3c00870
ACS Cent. Sci. 2023, 9, 2044−2056

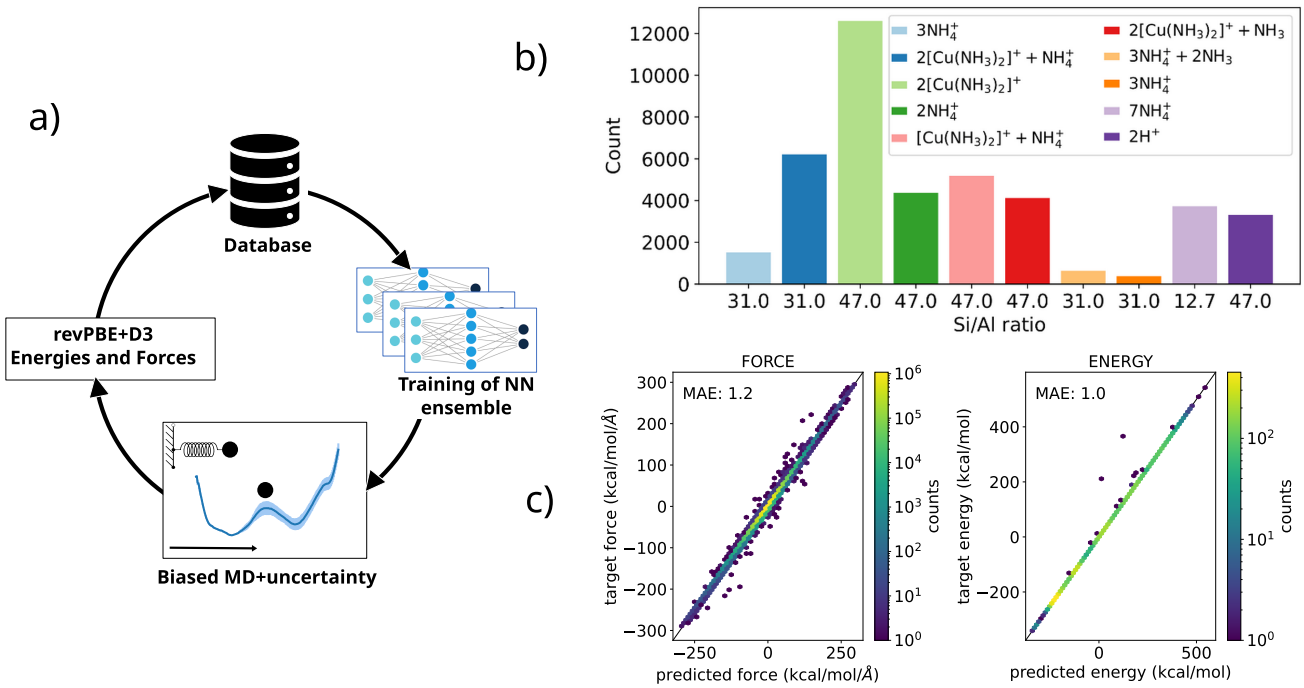

Figure 1. Neural network potential. (a) Illustration of the active learning cycle. At each iteration, an ensemble of NNPs is trained on the available labeled data contained in the database, initially obtained from previous PBE+D3 MD simulations. Then, biased MD trajectories are generated with these NNPs, and based on the force uncertainty of an ensemble of three NNPs, new geometries are collected, and their corresponding PBE+D3 energies and forces are computed and included in the data set. In the next loops, the newly generated data are combined with the existing data to train an updated NNP. (b) Distribution of the chemical composition of the 42K models included in the final data set, comprising models with Si/Al ratios of 13, 31 and 47, and with the negative charges arising from Al substitution compensated by $[Cu(NH_3)_2]^+$, NH_4^+, or H^+. (c) Correlation between the predicted and target energies (left) and forces (right) of the last-generation NNP.

$(NH_3)_2]^+$ monomers in the same *cha* cage. The hops between adjacent *cha* cages are modulated by size exclusion effects and also by the attractive interaction between the positively charged $[Cu(NH_3)_2]^+$ complexes and the negatively charged framework Al sites.[8,9,15,17,18] Thus, structural properties such as the Al content and distribution, Cu loading, and Brønsted acid site density as well as the interaction of the Cu active sites with the reactants, in particular, NH_3, might affect the mobility of Cu cations and consequently the NH_3−SCR−NO_x reaction rate. This has been evidenced by recent studies combining catalytic activity tests with *operando* XAS or EPR spectroscopy,[19−23] and *ab initio* molecular dynamics (AIMD) simulations have been successfully applied to provide atomistic insight into the dynamic nature of the Cu^+ cations under reaction conditions.[9,17,18]

The cost of AIMD simulations limits their applicability to a few selected systems at a time, at small length scales in the nanometer range and short time scales of ∼100 ps, while the faster classical force fields are not suited to describe the specific interactions involved in the systems investigated.[24] For these reasons, the systematic exploration of parameters such as the Si/Al ratio, Al distribution, Cu/Al ratio, NH_3 concentration, and the presence of Brønsted acid sites and compensating NH_4^+ cations has not yet been possible. Another possible avenue is to use machine learning potentials, which despite being slower than classical force fields allow access to the nanosecond scale.[25]

Machine learning (ML) has demonstrated broad applicability in materials science[26,27] and heterogeneous catalysis.[28−31] Machine learning potentials (MLPs), when trained with a sufficiently large and diverse data set, can match the accuracy of quantum chemistry methods at a fraction of the computational cost.[32−38] This allows the study of larger and more realistic systems and more complex scientific problems,[27,39−41] in particular, those requiring the use of molecular dynamics simulations.[42−44] A broad variety of MLPs based on neural networks, so-called neural network potentials (NNPs), have been developed in the last few years (ANI,[45−48] deep tensor neural networks,[49] SchNet,[50] DeepPotentialNet,[51] MEGNet,[52] DimeNet,[53] OrbNet,[54] PaiNN,[55] NequIP[56]) and have been successfully used to study solid systems,[40,57−59] ion diffusion,[60] and chemical reactions,[61−63] but the number of applications in the field of zeolite catalysis is still rather limited.[58,64,65]

Here, we leveraged these innovations and trained a NNP capable of describing $[Cu(NH_3)_2]^+$ species in aluminosilicate CHA with varying composition and NH_3 concentration. The trained NNP proved accurate and transferable, and acquiring all of the training data was less costly than one traditional AIMD simulation. Biased MD simulations reproduced free-energy profiles from DFT and provided insight into transport for over a dozen combinations of the Al distribution and the presence of NH_4^+. Unbiased MD simulations were scaled to thousands of atoms for nanoseconds and achieved a more realistic representation of the importance of Al density and distribution, Cu loading, and adsorbed NH_3 in the mobility of Cu^+ cations in Cu-CHA catalysts.

These results show that the activation free energy for $[Cu(NH_3)_2]^+$ hops between adjacent cages is lower for windows containing Al pairs but also that this is a local effect with only a weak influence on long-range mobility. $[Cu(NH_3)_2]^+$ migration to remote cages requires the simultaneous

https://doi.org/10.1021/acscentsci.3c00870
ACS Cent. Sci. 2023, 9, 2044−2056

Table 1. Chemical Composition, Cationic Species, and Molecules Included in the Triclinic $T_{96}O_{192}$ Supercell Models Used for Active Learning and Adversarial Attack

Formulas	Si/Al	Al	Si	$[Cu(NH_3)_2]^+$	NH_4^+	NH_3	H^+
$H_2Al_2O_{192}Si_{94}$	47	2	94	0	0	0	2
$H_8Al_2N_2O_{192}Si_{94}$	47	2	94	0	2	0	0
$H_{12}Al_3N_3O_{192}Si_{93}$	31	3	93	0	3	0	0
$H_{15}Al_3N_4O_{192}Si_{93}$	31	3	93	0	3	1	0
$H_{18}Al_3N_5O_{192}Si_{93}$	31	3	93	0	3	2	0
$H_{28}Al_7N_7O_{192}Si_{89}$	12.7	7	89	0	7	0	0
$H_{12}Al_2Cu_2N_4O_{192}Si_{94}$	47	2	94	2	0	0	0
$H_{10}Al_2Cu_1N_3O_{192}Si_{94}$	47	2	94	1	1	0	0
$H_{18}Al_2Cu_2N_6O_{192}Si_{94}$	47	2	94	2	0	2	0
$H_{16}Al_3Cu_2N_5O_{192}Si_{93}$	31	3	93	2	1	0	0

displacement of charge-compensating NH_4^+, which shows a lower mobility that is enhanced by excess NH_3. Finally, simulations with large supercells show that the probability of finding two $[Cu(NH_3)_2]^+$ complexes in the same cage, a prerequisite for the SCR-NOx reaction, increases with Cu loading and also with the Al content in the zeolite. We confirm these trends experimentally through catalytic tests of Cu-CHA samples with controlled Si/Al and Cu/Al ratios.

RESULTS AND DISCUSSION

Neural Network Potential. NNPs are highly accurate, but they struggle to extrapolate outside their training data. In order to ensure robust and accurate production simulations, our NNP was trained on data gathered through multiple generations of active learning (AL) using a query-by-committee approach.[66−74] A committee (ensemble) of NNPs was trained on the available labeled data at each iteration, and new data was collected based on the disagreement (variance) of the prediction of the committee members on newly generated geometries, as illustrated in Figure 1a. (See a more detailed description in the Methods section in the Supporting Information.) The first generation of the potential was trained on a randomly collected subset of the DFT data from a previous study[18] and from three biased simulations performed with DFT at 423 K, used as reference ground truth. In total, there were ∼9000 geometries in the initial data set. This pretrained potential was then retrained in four active learning loops using the 2 × 2 × 2 triclinic supercell described in the Methods section and depicted in Figure S1. For each loop, biased MD trajectories were generated with the learned interatomic potential of the previous loop at temperatures of 298, 423, 500, and 550 K. The selection of the new geometries from the MD trajectories was carried out using as a criterion the force uncertainty from an ensemble of three NNPs. The variances among the forces within the ensemble of potentials were ranked in descending order, and the first geometries were selected to increase the data set in 10%. The nonphysical geometries and those with low uncertainty, <2 kcal/mol, were discarded. Up to this point, the data set contained only structures with the $H_{12}Al_2Cu_2N_4O_{192}Si_{94}$ composition (see Table 1 and the light-green bar in Figure 1b), where the negative charges generated by framework Al atoms were always compensated with $[Cu(NH_3)_2]^+$ species so that the trained potential did not properly describe local environments of Al compensated with NH_4^+ or H^+. The acquisition of new geometries with new compositions including NH_4^+ and H^+ was performed using an adversarial attack[75] for six more generations with NNPs trained on the last generation of active learning. Systems with only two Al substitutions per unit cell (Si/Al = 47) were included in the data set to control the distribution of Al pairs in the 8MR windows and to provide specific environments for regions with low local Al concentration. Then, five more generations of active learning were used, with biased MD simulations at temperatures ranging from 600 to 1000 K to force larger deviations from the equilibrium structures, thus ensuring a better configurational sampling. The last generation of the NNP was trained on a complete data set containing 42K revPBE+D3 force calculations on structural models containing from 290 to 323 atoms per supercell, with a diverse set of atomic local environments in which the negative charges arising from Al substitution were compensated with $[Cu(NH_3)_2]^+$, NH_4^+, or H^+[75−77] as summarized in Table 1 and plotted in Figure 1b.

The active learning strategy was capable of automatically adding new, diverse, and informative chemical environments to the training pool at each of the preselected compositions through a combination of MD and uncertainty quantification. It generated informative training data for a number of chemical processes that occur during the reaction but were not present in the initial training data. These include adsorption and protonation of NH_3 on the Brønsted acid sites to form NH_4^+ cations, exchange between a gas-phase NH_3 molecule and one of the two NH_3 ligands of the $[Cu(NH_3)_2]^+$ complex, and proton transfer from NH_4^+ to NH_3. The diffusion of $[Cu(NH_3)_2]^+$ complexes through the 8R windows that connect adjacent *cha* cages has a higher activation barrier. Therefore, representative training data was obtained through the same enhanced sampling approach as the production simulations (Figure S2).

This strategic combination of biased MD with uncertainty quantification allowed efficient sampling of the relevant regions on the PES with a small and diverse number of DFT evaluations. Figure S3 illustrates the structural diversity in the final data set by means of a 2D projection of the local chemical environments around each Al atom in our data using UMAP[78] on the feature vectors learned by the NNP.[79] Atoms with similar local environments have similar feature vectors and appear close to the UMAP plot. The overlap among the chemical compositions suggests a nearly continuous sampling of the Al local environment.

Figure 1d shows the correlation between predicted and target energies and forces for a held-out test set. The mean absolute error of the predicted energies and forces are 0.98 and 1.2 kcal/mol/Å, respectively, indicating that the NNP is capable of predicting the energies and forces with chemical accuracy.

https://doi.org/10.1021/acscentsci.3c00870
ACS Cent. Sci. 2023, 9, 2044−2056

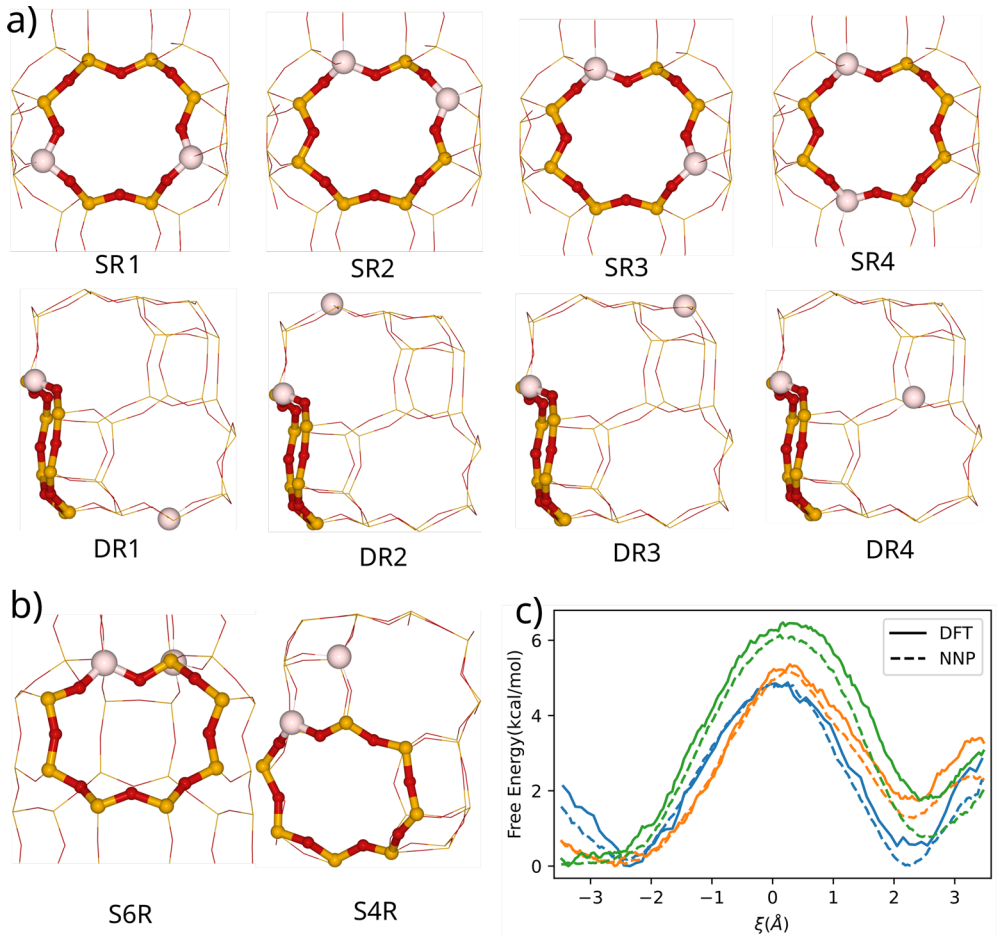

Figure 2. Structural models and accuracy of NNP biased simulations. (a, b) Representation of the different Al pair distributions used in the biased simulations. Si and O atoms are depicted as orange and red sticks, respectively. Al atoms are depicted as light-brown balls. The Si and O in the 8R window through which the $[Cu(NH_3)_2]^+$ complex diffuses are highlighted as orange and red balls. (c) Comparison of free-energy profiles for $[Cu(NH_3)_2]^+$ diffusion through the 8R window of SR1 (orange), SR4 (blue), and DR2 (green) systems obtained from DFT (solid line)- and NNP (dashed line)-based biased simulations at 423 K.

Effect of Al Distribution on $[Cu(NH_3)_2]^+$ Diffusion through 8R Windows from Biased Simulations. The favorable speed of the NNP accelerates US MD simulations by orders of magnitude over DFT, and it enabled a systematic exploration of the role of Al distribution in well-converged simulations. Ten different structural models with the same $H_{12}Al_2Cu_2N_4O_{192}Si_{94}$ composition corresponding to Si/Al = 47 but with different Al distributions were built (Figure 2a,b). The two Al atoms were placed either in the same 8R window (structures labeled SR1, SR2, SR3, and SR4), in different 8R windows (structures labeled DR1, DR2, DR3, and DR4) in the same 4R (S4R), or in the same 6R (S6R), and each framework Al was compensated with a $[Cu(NH_3)_2]^+$ cationic complex (entry 7 in Table 1).

Because the error of the predicted forces is not a sufficient metric for true performance in production simulations,[25] the NNPs were further validated by comparing NNP and DFT free-energy profiles for $[Cu(NH_3)_2]^+$ diffusion through the 8R window of SR1, SR4, and DR2 models. Due to the high computational cost of producing reference DFT biased simulations, a smaller hexagonal 126-atom unit cell was used. The free-energy profiles for SR1, SR4, and DR2 (Figure 2c) and the activation free energies (ΔF_{act}) calculated as the energy difference between the maximum and the minimum on the profile, 5.2 and 5.3 kcal/mol for SR1, 4.8, and 4.8 kcal/mol for SR4, and 6.1 and 6.4 kcal/mol for DR2, are in excellent agreement at both computational levels.

The smoother NNP traces are a consequence of more abundant sampling (4.8 ns total as compared to 0.8 for DFT) given the advantageous computational cost of NNPs (20 ps of AIMD required over a week on CPU Intel(R) Xeon(R) E5-2650 cores as compared to 20 min on a Tesla V100-32 GB GPU for NNPs).

Then, the free-energy profiles for $[Cu(NH_3)_2]^+$ diffusion between neighboring cages in the 10 systems depicted in Figure 2a,b were obtained from NNP biased simulations at 423 K using the larger $H_{12}Al_2Cu_2N_4O_{192}Si_{94}$ models. The profiles are plotted in Figure 3, and the corresponding values of activation (ΔF_{act}) and reaction (ΔF) free energies are summarized in Table S1. The shaded area in each profile shows the standard error calculated from three independent simulations using three different NNPs trained on the same data set. The average value of the standard error, 0.1 kcal/mol in all cases, indicates a low uncertainty in the prediction of the free energy and well-converged statistics.

For the systems with two Al atoms in the same 8R (orange profiles in Figure 3a), ΔF_{act} values range from 3.9 to 5.4 kcal/mol and the reaction is slightly endergonic with ΔF values between 0.4 and 2.3 kcal/mol. In all other cases, ΔF_{act} is higher than 6 kcal/mol and ΔF is larger than 3 kcal/mol, with the

https://doi.org/10.1021/acscentsci.3c00870
ACS Cent. Sci. 2023, 9, 2044−2056

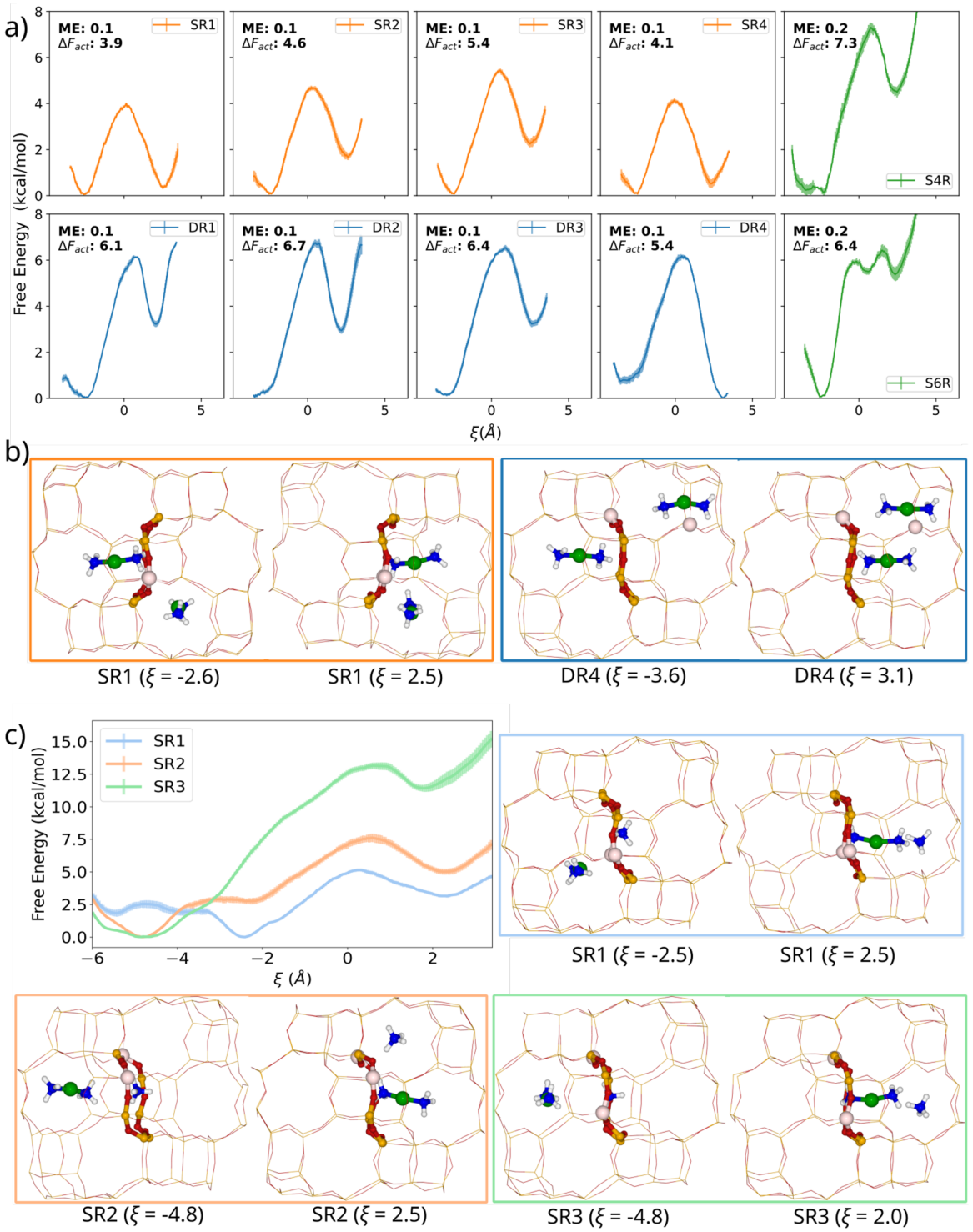

Figure 3. NNP biased simulations of $[Cu(NH_3)_2]^+$ diffusion. (a) Free-energy profiles for the diffusion of one $[Cu(NH_3)_2]^+$ complex from cage A to neighboring cage B occupied by another $[Cu(NH_3)_2]^+$ complex. (b) Snapshots of the initial and final minimum states corresponding to the diffusion of $[Cu(NH_3)_2]^+$ through the 8R windows of SR1 and DR4 systems at 423 K. (c) Free-energy profiles for $[Cu(NH_3)_2]^+$ diffusion between neighboring cages in the presence of one NH_4^+ cation initially placed in the 8R to be crossed in three systems with different Al distributions obtained from NNP-based biased simulations at 423 K and snapshots of the initial and final minimum states in the systems SR1, SR2, and SR3. Si, O, Al, H, Cu, and N atoms are depicted in orange, red, light brown, white, green, and blue, respectively. The atoms in the 8R window through which $[Cu(NH_3)_2]^+$ diffuses are highlighted.

only exception of the DR4 system for which the process is slightly exergonic. The Al distribution in the DR4 model is the same as in the SR1 model, but the diffusion of the $[Cu(NH_3)_2]^+$ complex proceeds through different 8R windows of the same model, highlighted in Figure 3b. In both cases, the stability of the final state with the two $[Cu(NH_3)_2]^+$ complexes in the same cage is similar to that of the initial state with the two complexes in different cages, which suggests that this

https://doi.org/10.1021/acscentsci.3c00870
ACS Cent. Sci. 2023, 9, 2044−2056

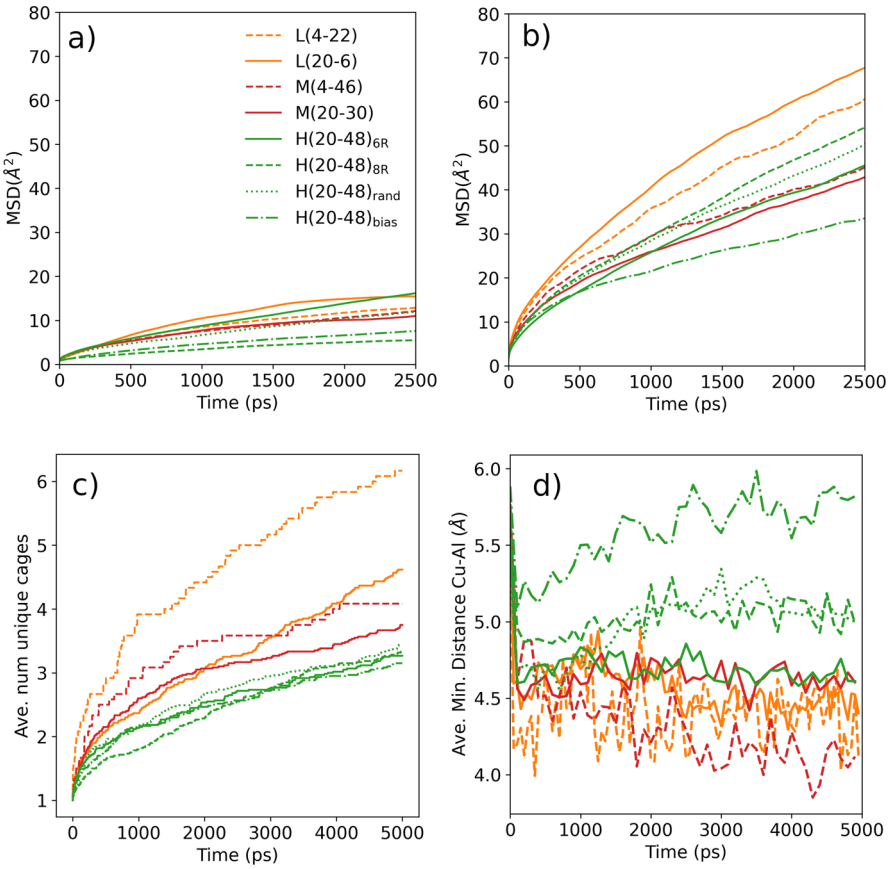

Figure 4. Mobility of NH_4^+ and $[Cu(NH_3)_2]^+$. (a) Mean square displacement (MSD) of the N atoms in NH_4^+ and (b) MSD of the Cu atoms in the $[Cu(NH_3)_2]^+$ complexes obtained from NPP-based unbiased MD simulations at 500 K. (c) Number of distinct cages visited by the Cu atoms. The apparent contradiction with the MSD plots is explained by the fact that the diffusion of $[Cu(NH_3)_2]^+$ does not occur along a preferential direction. One Al pair in an 8R can accelerate the diffusion of $[Cu(NH_3)_2]^+$ between two neighboring cages in multiple forward and backward steps so that only two distinct cages are visited by this complex. (d) Average minimum Cu−Al distances. All plots were obtained from the same simulations. See the Supporting Information for details on the calculation of MSD.

particular Al distribution might favor the formation of the $[Cu(NH_3)_2]^+$−OO−$[Cu(NH_3)_2]^+$ dimers involved in the low-temperature NH_3−SCR−NOx reaction. In contrast, distributions with two Al atoms in the same 4R or 6R hinder the formation of such dimeric intermediates because only one of the two $[Cu(NH_3)_2]^+$ complexes can stay near the Al atoms, while the second $[Cu(NH_3)_2]^+$ is forced to remain too close to the first, resulting in its diffusion through a different 8R to another empty cage. These results demonstrate that the Al distribution affects the movement of $[Cu(NH_3)_2]^+$ species between cages and the stability of pairs of $[Cu(NH_3)_2]^+$ complexes in the same cage and points to a positive effect of Al pairs in 8R on the rate of the low-temperature NH_3−SCR−NOx reaction.

Effect of NH_4^+ on the Diffusion of $[Cu(NH_3)_2]^+$ through 8R Windows from Biased Simulations. The mobility of $[Cu(NH_3)_2]^+$ complexes within the zeolite microporous structure is affected by the presence of other molecules involved in the reaction, among which NH_3 is the most abundant and the one with the largest impact on diffusion and reactivity.[17,18,21,22,80,81] Under reaction conditions, NH_3 is readily protonated on the Brønsted acid sites forming NH_4^+ cations that remain coordinated to the framework AlO_4^- units and might partly block the diffusion of $[Cu(NH_3)_2]^+$ complexes through the 8R windows. To analyze this possibility, we first performed NNP biased simulations at 423 K using the previously described $H_{10}Al_2Cu_1N_3O_{192}Si_{94}$ models with two framework Al atoms compensated now with one $[Cu(NH_3)_2]^+$ complex initially placed in the center of cavity A (see Figure S2) and one NH_4^+ cation initially placed in the plane of the 8R through which $[Cu(NH_3)_2]^+$ will diffuse. The free-energy profiles obtained for the three Al distributions considered (SR1, SR2, and SR3), as plotted in Figure 3c, are clearly different from those depicted in Figure 3a, and the calculated activation free energies for $[Cu(NH_3)_2]^+$ diffusion are also reflective of how the strong coordination of NH_4^+ modifies transport.

In the previous simulations without NH_4^+ the most stable minimum for the initial state occurs at $\xi \approx -2.5$ Å, with $[Cu(NH_3)_2]^+$ relatively close to the 8R, which is the case only for SR1 in the presence of NH_4^+ (blue profile in Figure 3c). In SR2 and SR3 models (orange and green profiles), the most stable minimum lies at $\xi \approx -4.8$ Å, with the $[Cu(NH_3)_2]^+$ complex closer to the center of the cavity and at a larger distance from the 8R to be crossed. The calculated ΔF_{act}, 5.2, 7.6, and 13.1 kcal/mol for SR1, SR2, and SR3, respectively, and ΔF values, 3.2, 5.0, and 11.4 kcal/mol for SR1, SR2, and SR3, respectively, are higher than those obtained for the corresponding systems in the absence of NH_4^+. The snapshots of the final state at $\xi \approx 2.5$ Å for SR1 and SR2 in Figure 3c show that the NH_4^+ cation has been displaced from its initial position in the plane of the 8R to a position relatively close to

https://doi.org/10.1021/acscentsci.3c00870
ACS Cent. Sci. 2023, 9, 2044−2056

one of the AlO_4^- units. In SR3, however, the NH_4^+ cation has been displaced to the opposite side of the cage, far from the two AlO_4^- sites present in the model, which would explain the instability of the system. The deviation across replicate profiles is wider in some regions, which we attribute to the fact that our simulations occasionally, but not exhaustively, sample the spontaneous reversible deprotonation of NH_4^+ cations to form NH_3 and a Brønsted acid site, which is typically not accessible to traditional simulations.

Altogether, the results from the biased simulations suggest a potential blocking effect of the NH_4^+ cations. However, their own mobility, as either NH_4^+ or NH_3 following proton transfer to deprotonated AlO_4^-, and possible migration from the 8R toward other nearby AlO_4^- units that are not present in this model might modify this conclusion. The NNPs developed here open the possibility of running long-time unbiased MD simulations on larger systems with more realistic chemical compositions, allowing one to capture the dynamics of $[Cu(NH_3)_2]^+$ and NH_4^+ globally and to observe long-range diffusion of both cationic species.

Long-Range Diffusion of NH_4^+ and $[Cu(NH_3)_2]^+$ Species from Unbiased MD Simulations. A large $T_{768}O_{1536}$ supercell with a dimension of ∼37 Å was used to construct eight models representing three Al contents, low (L, Si/Al ≈ 30) with 26 Al atoms in the unit cell, medium (M, Si/Al ≈ 14) with 50 Al atoms in the unit cell, and high (H, Si/Al ≈ 10) with 68 Al atoms in the unit cell, as described in detail in the Methods section and Figure S4 in the Supporting Information. The framework Al were compensated with combinations of $[Cu(NH_3)_2]^+$, NH_4^+, and H^+ as summarized in Table S2. Each model's name contains a letter indicating the Al content (L, M, or H) followed by two numerical values indicating the number of $[Cu(NH_3)_2]^+$ and NH_4^+ compensating cations. Thus, L(20-6) indicates low Al content, with 26 Al atoms in the unit cell compensated with $20[Cu(NH_3)_2]^+$ and $6NH_4^+$ cations. Unbiased MD simulations were conducted for at least 5 ns on each ∼2000-atom system using a slightly higher *T*, 500 K, in order to enhance the mobility of the $[Cu(NH_3)_2]^+$ cations and increase the probability of hopping events between neighboring cavities.

Figure 4a,b tracks the time evolution of the mean square displacements (MSDs) of the N atoms in the NH_4^+ cations and of the Cu atoms in the $[Cu(NH_3)_2]^+$ complexes, respectively. While both species have a net charge of +1, $[Cu(NH_3)_2]^+$ is much more mobile while NH_4^+ cations are more closely attached to the AlO_4^- units (Figures S5 and S6). This is because the positive charge in the $[Cu(NH_3)_2]^+$ complexes is highly shielded by the two NH_3 ligands.

The similarity among the MSD profiles of N atoms suggests that the mobility of NH_4^+ cations is rather independent of the zeolite framework composition and Cu content (Figure 4a), while the MSD traces for Cu (Figure 4b) suggest slightly lower mobility of $[Cu(NH_3)_2]^+$ in the systems with high Al content (Si/Al ≈ 10, Figure 4b). The trends are similar in the number of distinct cages visited by the $[Cu(NH_3)_2]^+$ complex over time (Figure 4c), but they are more stratified and more clearly show an increase in mobility with decreasing copper content (orange and red dashed lines higher than solid lines in Figure 4c). In 5 ns, each $[Cu(NH_3)_2]^+$ complex visits on average fewer than three different cages in the models with high Al content, which increases to three to four for intermediate Al and reaches a maximum of over five different cages visited for the L4 model, which has the lowest Al content and thus few Al pairs in 8R. This is in apparent contradiction to the biased simulation results for small models, which showed a lower hopping free-energy barrier for Al pairing in 8R. A potential explanation is that the hopping landscape is statically and dynamically heterogeneous, with the local chemical environment of each initial and final cage and transient cage occupation by other mobile molecules influencing the mobility of copper complexes. Figure S5 shows the diversity in length and tortuosity in example trajectories of Cu atoms inside the zeolite microporous structure. While MSD profiles representing the average movement of the $[Cu(NH_3)_2]^+$ species are relatively similar across catalyst models (∼40−60 $Å^2$), the local mobility of each individual $[Cu(NH_3)_2]^+$ complex depends on its local chemical environment.

Once the influence of Al content was established, we analyzed the effect of NH_4^+ on the mobility of $[Cu(NH_3)_2]^+$ complexes in systems with a constant Si/Al ratio. Increasing the amount of NH_4^+ from 30 to 46 cations (compare M(20−30) with M(4−46) models in Figure 4c) or from 6 to 22 cations (compare L(20−6) with L(4−22) in Figure 4c) increases the number of cages visited, suggesting a positive effect of NH_4^+ on the long-range diffusion of $[Cu(NH_3)_2]^+$. A proposed explanation is that adsorbed NH_4^+ shields the attractive interaction between the AlO_4^- anionic sites and the $[Cu(NH_3)_2]^+$ complexes. Each NH_4^+ forms two strong hydrogen bonds with the AlO_4^- site, hence the lower mobility of NH_4^+, while $[Cu(NH_3)_2]^+$ interacts with the zeolite through the H atoms of the coordinating NH_3 molecules. This "crowding" of the anionic sites by the harder NH_4^+ can be observed statistically in the simulations. The average distances between the Cu atoms and the closest framework Al atoms plotted in Figure 4d are ∼4.5 Å in the L and M models (orange and red lines) and increase to ∼5.0 Å in the systems with higher Al content and thus a larger amount of charge-balancing NH_4^+ (green lines). The $H(20-48)_{bias}$ model has a heterogeneous Al distribution, and its anomalously high Cu−Al distance is due to $[Cu(NH_3)_2]^+$ complexes in Al-poor regions.

Previous studies have suggested that $[Cu(NH_3)_2]^+$ migration is fast only among the three cages sharing a common framework Al, while long-range diffusion to nonadjacent cages is limited to ∼9 Å due to the decaying electrostatic interaction between the $[Cu(NH_3)_2]^+$ and the anionic AlO_4^- site.[9,18,20] This argument is rigorously true when the final cages contain no additional Al sites, as in our model systems from the first section. In real systems, however, the long-range diffusion is easily explained through a sequence of local steps combining the crossing of 8R windows into adjacent Al-containing cages, followed by the exchange of NH_4^+ as a compensating cation (Scheme S1 in the Supporting Information). The low mobility of NH_4^+ revealed by the present simulations suggests that a limiting factor for such long-range diffusion of $[Cu(NH_3)_2]^+$ complexes is the slower rate of countermigration of the charge-compensating NH_4^+. While $[Cu(NH_3)_2]^+$ could act as a migrating compensating cation, this results in no net migration of Cu.

To explore this hypothesis, two additional MD simulations of 5 ns were run using two modified M20 models, one of them containing 30 protons as compensating cations, labeled as M20-H+, and another one with 60 additional NH_3 molecules added to the system, labeled as M20-NH3. Protons on the Brønsted acid sites are fairly static and localized within the four oxygen atoms directly attached to Al, so the long-range charge-

https://doi.org/10.1021/acscentsci.3c00870
ACS Cent. Sci. 2023, 9, 2044−2056

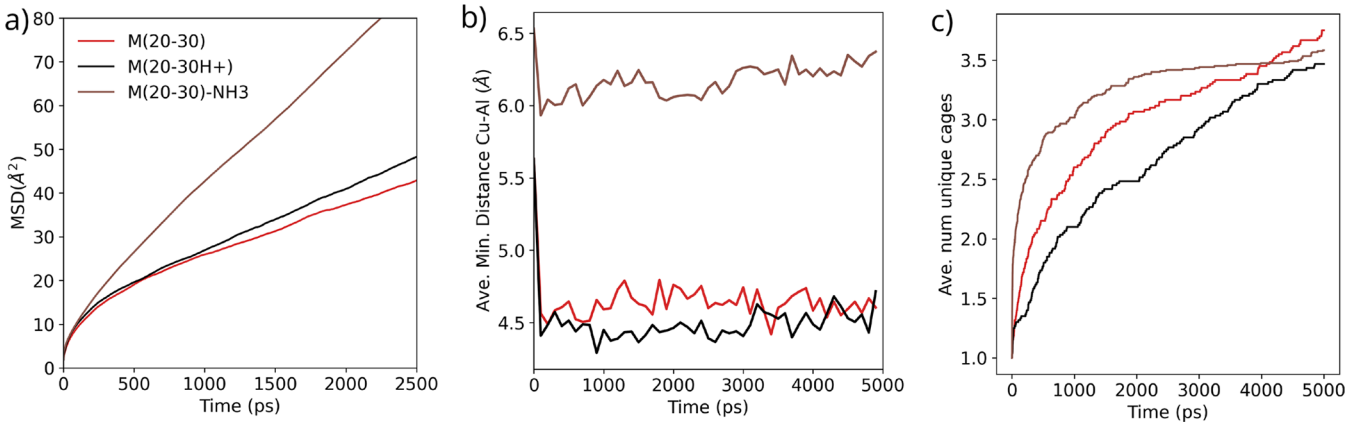

Figure 5. Influence of framework charge shielding on the mobility of $[Cu(NH_3)_2]^+$. (a) Mean square displacement (MSD) of Cu atoms in the $[Cu(NH_3)_2]^+$ complexes, (b) average minimum Cu−Al distances, and (c) number of distinct cages visited obtained from NPP-based unbiased MD simulations at 500 K in models with different charge-compensating cations and additional NH_3 molecules. See the Supporting Information for details on the calculation of MSD.

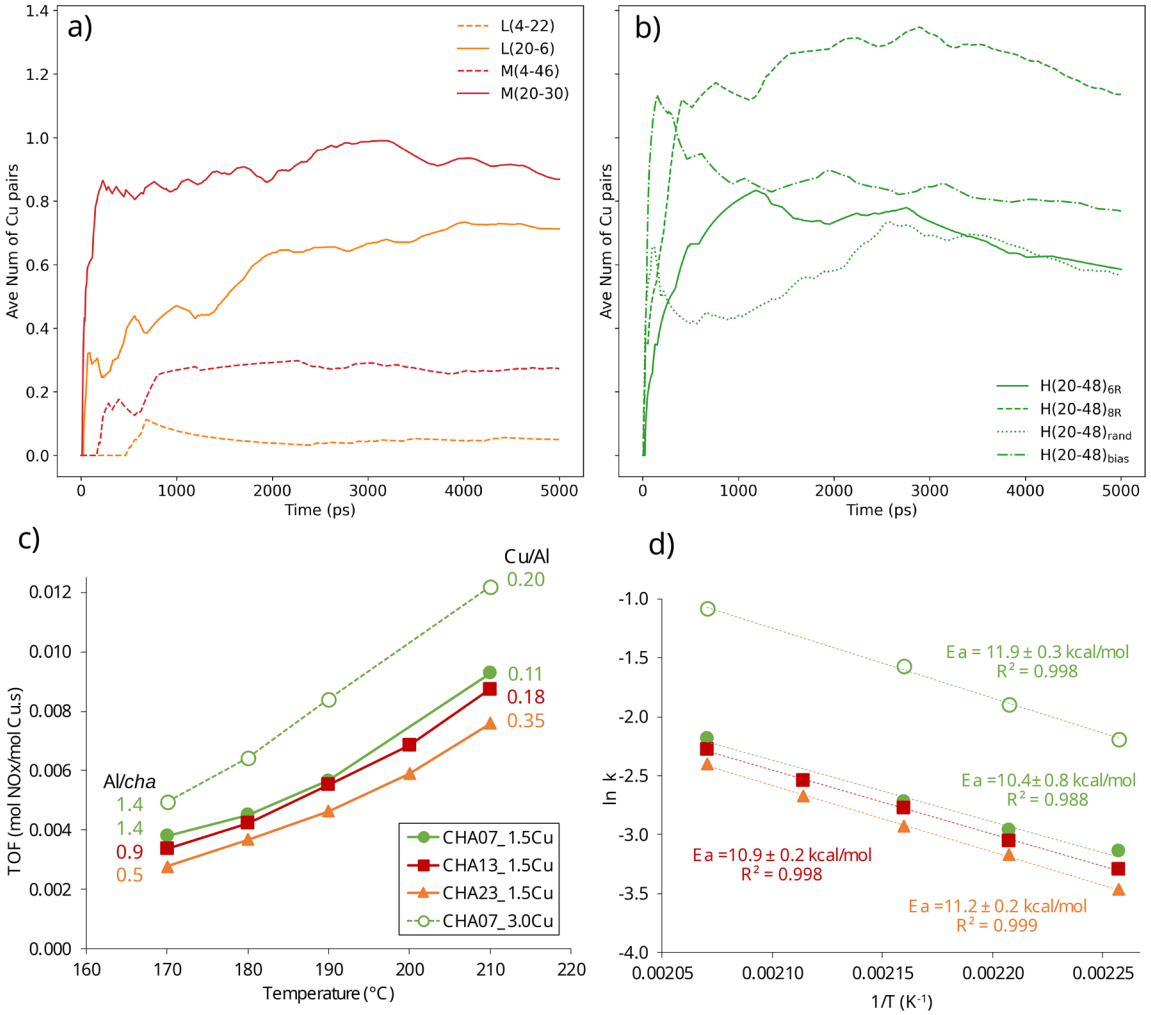

Figure 6. Probability of formation of the active sites and catalytic results for the NH_3-SCR-NOx reaction. (a,b) Time evolution of the average number of $[Cu(NH_3)_2]^+$ pairs in the same cage for the eight systems in Figure S4. The geometric centers of every cage in the unit cell are determined, and two Cu atoms are considered to be in the same cage when both have the same cage center as the nearest cage center. (c) Turnover frequency (TOF) values on a per Cu ion basis for the ∼1.5 wt % Cu-containing zeolites with different Si/Al molar ratios and the CHA07 sample (Si/Al ≈ 7) with two different Cu contents (∼1.5 and ∼3 wt % Cu). (d) Arrhenius plots for the same experiments including the corresponding values of apparent activation energy obtained from the slope of each plot.

https://doi.org/10.1021/acscentsci.3c00870
ACS Cent. Sci. 2023, 9, 2044−2056

compensation diffusion of H^+ should be hindered. In contrast, additional NH_3 should facilitate the movement of the positive charges via proton transfer from NH_4^+ to NH_3 via a Grotthuss-like chain of proton transfers, thus allowing faster charge compensation between separated AlO_4^- units without the need to physically displace the strongly attached NH_4^+ cations.

The plots in Figure 5 confirm this hypothesis. The MSD of Cu atoms in Figure 5a does not change when NH_4^+ cations are substituted by protons (black lines) with a similar electrostatic shielding effect as NH_4^+. However, the Cu mobility increases significantly in the presence of excess NH_3 molecules (brown lines), suggesting that free NH_3 facilitates the charge re-equilibrium following $[Cu(NH_3)_2]^+$ crossing 8R. The average distances between the Cu atoms and the closest framework Al atoms increase from ∼4.5 to ∼6.0 Å with the added NH_3 (Figure 5b). Finally, the number of distinct cages visited by $[Cu(NH_3)_2]^+$ (Figure 5c) indicates again a slightly lower long-range mobility of $[Cu(NH_3)_2]^+$ in the model containing Brønsted acid sites and enhanced diffusion in the presence of an excess of NH_3.

Our results provide theoretical backing to recent experimental observations of the enhancing effect of gas-phase NH_3 during the solid-state ion exchange of copper using mixtures of copper oxides and zeolites, which allows the fast preparation of Cu-exchanged zeolites at low temperatures (473−523 K).[80,81] After ∼4000 ps, the three models reached similar steady states with ∼3.5 distinct cages being visited by each complex, corresponding to the final state of the ion-exchange process with a random distribution of $[Cu(NH_3)_2]^+$ complexes occupying the whole unit cell.

Bimolecular Complexes and Mechanistic Implications for the NH_3−SCR−NOx Reaction. According to the proposed mechanism,[9] the reaction rate depends directly on the number of dimeric intermediates formed by the pairing of two $[Cu(NH_3)_2]^+$ complexes in the same cage. Figure 6a,b tracks the time evolution of the average number of $[Cu(NH_3)_2]^+$ pairs, that is, two $[Cu(NH_3)_2]^+$ ions simultaneously in the same cage, formed in each of the eight models analyzed in the previous section. As expected,[9,19,20] the number of $[Cu(NH_3)_2]^+$ pairs depends directly on the total amount of Cu in the system (compare yellow and red dashed lines with yellow and red full lines). More interestingly, for a given Cu content, the number of $[Cu(NH_3)_2]^+$ pairs formed along the simulation is systematically larger in the systems with higher Al content, in agreement with recent work by Krishna et al. showing that the fraction of Cu^+ cations that can be oxidized by O_2 increases with increasing Al content in Cu-CHA zeolites of varying composition.[20] On the other hand, the four models with the same Cu content, same Si/Al ratio of ∼10, and different Al distributions $H(20-48)_{6R}$, $H(20-48)_{8R}$, $H(20-48)_{rand}$, and $H(20-48)_{bias}$ (see Methods section, Figure S4, and Table S2) exhibit quite similar but not fully equivalent behavior. The time evolution plots in Figure 6b suggest a higher probability of $[Cu(NH_3)_2]^+$ pairing in the $H(20-48)_{8R}$ models containing two framework Al atoms in the same 8R, in agreement with the lower activation free energies (ΔF_{act}) obtained for $[Cu(NH_3)_2]^+$ diffusion through these Al-pair-containing 8R windows.

Experimental Validation for the Low-T NH_3-SCR-NOx Reaction Catalyzed by Cu-CHA Zeolites with Controlled Composition. To experimentally validate the computational predictions, three CHA samples with different Si/Al molar ratios ranging from 7.3 to 23.3, which translates to a broad range of 1.4 to 0.5 Al sites per *cha* (see Table S3 in the Supporting Information) were synthesized as described in the Methods section. Then, the same Cu loading (∼1.5 wt % Cu) was introduced within the three CHA materials, which resulted in a similar amount of initial Cu atoms per *cha* cage, ∼0.17, but different Cu/Al ratios (from 0.11 to 0.35, see Table S4). In addition, the CHA sample with a Si/Al ratio of ∼7.3 was also loaded with 3.0 wt % Cu, resulting in an additional sample with an increased number of initial Cu atoms per *cha* cage (0.3). The Si/Al ratios in these samples and in the industrial catalysts are lower than those considered in some systems of the training data set and in some simulations. The reason is that in macroscopic systems the Al atoms are not uniformly distributed along the crystal, and the training of the NNP should include local environments with higher and lower Si/Al ratios to avoid extrapolations.

The catalytic tests to evaluate the low-temperature SCR-NOx activity of the different Cu-CHA materials were performed at very high space velocities (1800000 mL/h·g of catalyst) to ensure low NO conversions (<20%). Turnover frequency values (TOF) were obtained for each Cu-CHA sample at five different temperatures (Figure 6c). The TOF values obtained for the three catalysts with different Si/Al molar ratios and the same Cu content (∼1.5 wt % Cu) exhibit a continuous activity enhancement as the Al/*cha* cage ratio increases from 0.5 to 1.4 (see Figure 6c), in agreement with the theoretical conclusion that the probability of simultaneously finding two $[Cu(NH_3)_2]^+$ complexes in the same *cha* cage increases with increasing the Al content in the zeolite. A comparison of the TOF values obtained for samples with the same Si/Al ratio and different Cu content (full and dotted green lines in Figure 6c) or even with similar Cu/Al ratios and different Cu content (red and dotted green lines in Figure 6c) confirms that the catalytic activity clearly improves with increasing the Cu/*cha* ratio, in good agreement with the theoretical conclusion that the probability of forming $[Cu(NH_3)_2]^+$ pairs in the same *cha* cage directly correlates with the total amount of Cu in the system.

The experimental apparent activation energies (Figure 6d) are similar for all samples irrespective of the Si/Al ratio, Cu content, or catalytic activity, ranging from 10.4 ± 0.8 to 11.9 ± 0.3 kcal/mol. The catalytic activity measured by the TOF and normalized by Cu content, however, increases in parallel with the calculated likelihood of two copper encounters in the same cage (Figure 6a,b). This supports the argument that the formation of $[Cu(NH_3)_2]^+$ pairs in the same *cha* cage is responsible for the generation of the binuclear active sites that catalyze the reaction, although copper diffusion may not necessarily be the rate-determining step of the global process.

■ CONCLUSIONS

Biased and unbiased MD simulations using a newly trained NNP have achieved high accuracy, chemical diversity, and good length and time scales, allowing the systematic investigation of the influence of catalyst composition and adsorbed NH_3 on the mobility of $[Cu(NH_3)_2]^+$ cations in Cu-CHA catalysts.

Biased simulations on small systems showed that single $[Cu(NH_3)_2]^+$ cation hops between adjacent *cha* cages are very sensitive to the Al distribution, and in general, Al pairs in 8R windows lower the free-energy barrier for diffusion and stabilize the product configuration with two $[Cu(NH_3)_2]^+$ cations in the same cage. This might be taken to suggest

https://doi.org/10.1021/acscentsci.3c00870
ACS Cent. Sci. 2023, 9, 2044−2056

that the rate of the SCR-NOx reaction could be accelerated by selectively positioning the Al atoms as Al pairs. However, even though those results are well beyond the limits of traditional AIMD, the simulation cells employed are overly simple and lack realistic Al and NH_4^+ concentrations.

Unbiased MD simulations using time scales of multiple nanoseconds and supercells with over 2300 framework atoms at a variety of Si/Al ratios and Cu^+, NH_4^+, and NH_3 loadings show that $[Cu(NH_3)_2]^+$ cations can visit on average 3 to 4 cages and diffuse as far as 30 Å in a few nanoseconds. They also show that long-range migration to remote cages requires the simultaneous displacement of a charge-compensating NH_4^+ cation. An excess of NH_3 facilitates the movement of the positive charges via proton transfer from NH_4^+ to NH_3, thus enhancing the long-range diffusion of $[Cu(NH_3)_2]^+$ complexes.

Regarding catalytic activity, we observed that the probability of finding two $[Cu(NH_3)_2]^+$ complexes in the same cage, which is necessary for the SCR-NOx reaction at low temperature, correlates directly with the Cu content and the Al content but not so much with the Al distribution. These trends were confirmed experimentally through testing the SCR-NOx reaction at low temperatures using Cu-CHA zeolites with different Si/Al and Cu/Al molar ratios, where we found increasing catalytic performance with increasing Al and Cu loading.

These results demonstrate the power of combining high-throughput DFT calculations, machine learning, and molecular dynamics simulations for simulating transport in nanoporous catalysts. The collection of the training data and the training of the NNP had a lower total computational cost than a single traditional AIMD simulation and resulted in scalable, fast, and accurate simulations.

This overall strategy is broadly applicable to other unsolved questions in nanoporous catalysts since it enables DFT accuracy and nanosecond-long MD simulations for thousands of atoms and possibly beyond by combining ML and enhanced sampling techniques.[82]

■ ASSOCIATED CONTENT

Data Availability Statement

The experimental and computational data that support the findings of this study are available from the corresponding author upon reasonable request. The data sets generated during this study are available at https://figshare.com/projects/Dataset_and_machine_learning_potential_Cu-CHA/167645. The code used for this study can be downloaded from https://github.com/learningmatter-mit/NeuralForceField.

Supporting Information

The Supporting Information is available free of charge at https://pubs.acs.org/doi/10.1021/acscentsci.3c00870.

Models, methods, and experimental section; Tables S1 to S4 with calculated energies, chemical compositions, and characterization of the experimental samples; Figures S1 to S8 showing the models, the collective variable, diffusion geometries, and trajectories; PXRD and FESEM characterization (PDF)

■ AUTHOR INFORMATION

Corresponding Authors

Mercedes Boronat − *Instituto de Tecnología Química, Universitat Politècnica de València-Consejo Superior de Investigaciones Científicas, 46022 Valencia, Spain;* orcid.org/0000-0002-6211-5888; Email: boronat@itq.upv.es

Rafael Gomez-Bombarelli − *Department of Materials Science and Engineering, Massachusetts Institute of Technology, Cambridge, Massachusetts 02139, United States;* orcid.org/0000-0002-9495-8599; Email: rafagb@mit.edu

Authors

Reisel Millan − *Department of Materials Science and Engineering, Massachusetts Institute of Technology, Cambridge, Massachusetts 02139, United States; Instituto de Tecnología Química, Universitat Politècnica de València-Consejo Superior de Investigaciones Científicas, 46022 Valencia, Spain;* orcid.org/0000-0002-4489-5411

Estefanía Bello-Jurado − *Instituto de Tecnología Química, Universitat Politècnica de València-Consejo Superior de Investigaciones Científicas, 46022 Valencia, Spain*

Manuel Moliner − *Instituto de Tecnología Química, Universitat Politècnica de València-Consejo Superior de Investigaciones Científicas, 46022 Valencia, Spain;* orcid.org/0000-0002-5440-716X

Complete contact information is available at: https://pubs.acs.org/10.1021/acscentsci.3c00870

Notes

The authors declare no competing financial interest.

■ ACKNOWLEDGMENTS

R.M. acknowledges the Margarita Salas grant from the Ministerio de Universidades, Spain, funded by the European Union-Next Generation EU. The authors are grateful for computation time allocated on the MIT SuperCloud cluster, the MIT Engaging cluster at the Massachusetts Green High Performance Computing Center (MGHPCC), and Summit at the Oakridge Leadership Computing Facility through the 2021 ALCC DOE program. R.G-B. thanks the Jeffrey Cheah Career Development Chair. R.M thanks Gavin Winter for assistance during the training of NNP and processing of the MD simulations and Simon Axelrod for implementing PaiNN. M.B. and M.M. are grateful for financial support from the Spanish government through PID2020-112590GB-C21, PID2021-122755OB-I00, and TED2021-130739B-I00 (MCIN/AEI/FEDER, UE) and from CSIC through the I-link+ Program (LINKA20381). E.B.-J. acknowledges the Spanish government-MCIU for a FPI scholarship (PRE2019-088360). The Electron Microscopy Service of the UPV is acknowledged for help with sample characterization.

■ REFERENCES

(1) Sushkevich, V. L.; Palagin, D.; Ranocchiari, M.; Van Bokhoven, J. A. Selective anaerobic oxidation of methane enables direct synthesis of methanol. *Science* **2017**, *356*, 523−527.

(2) Dinh, K. T.; Sullivan, M. M.; Narsimhan, K.; Serna, P.; Meyer, R. J.; Dincă, M.; Román-Leshkov, Y. Continuous Partial Oxidation of Methane to Methanol Catalyzed by Diffusion-Paired Copper Dimers in Copper-Exchanged Zeolites. *J. Am. Chem. Soc.* **2019**, *141*, 11641−11650.

(3) Dinh, K. T.; Sullivan, M. M.; Serna, P.; Meyer, R. J.; Román-Leshkov, Y. Breaking the Selectivity-Conversion Limit of Partial Methane Oxidation with Tandem Heterogeneous Catalysts. *ACS Catal.* **2021**, *11*, 9262−9270.

(4) Del Campo, P.; Martínez, C.; Corma, A. Activation and conversion of alkanes in the confined space of zeolite-type materials. *Chem. Soc. Rev.* **2021**, *50*, 8511−8595.
(5) Ohyama, J.; Tsuchimura, Y.; Hirayama, A.; Iwai, H.; Yoshida, H.; Machida, M.; Nishimura, S.; Kato, K.; Takahashi, K. Relationships among the Catalytic Performance, Redox Activity, and Structure of Cu-CHA Catalysts for the Direct Oxidation of Methane to Methanol Investigated Using In Situ XAFS and UV-Vis Spectroscopies. *ACS Catal.* **2022**, *12*, 2454−2462.
(6) Kwak, J. H.; Tonkyn, R. G.; Kim, D. H.; Szanyi, J.; Peden, C. H. F. Excellent activity and selectivity of Cu-SSZ-13 in the selective catalytic reduction of NOx with NH3. *J. Catal.* **2010**, *275*, 187−190.
(7) Paolucci, C.; Parekh, A. A.; Khurana, I.; Di Iorio, J. R.; Li, H.; Albarracin Caballero, J. D.; Shih, A. J.; Anggara, T.; Delgass, W. N.; Miller, J. T.; Ribeiro, F. H.; Gounder, R.; Schneider, W. F. Catalysis in a cage: Condition-dependent speciation and dynamics of exchanged cu cations in ssz-13 zeolites. *J. Am. Chem. Soc.* **2016**, *138*, 6028−6048.
(8) Gao, F.; Mei, D.; Wang, Y.; Szanyi, J.; Peden, C. H. Selective Catalytic Reduction over Cu/SSZ-13: Linking Homo- and Heterogeneous Catalysis. *J. Am. Chem. Soc.* **2017**, *139*, 4935−4942.
(9) Paolucci, C.; Khurana, I.; Parekh, A. A.; Li, S.; Shih, A. J.; Li, H.; Di Iorio, J. R.; Albarracin-Caballero, J. D.; Yezerets, A.; Miller, J. T.; Delgass, W. N.; Ribeiro, F. H.; Schneider, W. F.; Gounder, R. Dynamic multinuclear sites formed by mobilized copper ions in NO x selective catalytic reduction. *Science* **2017**, *357*, 898−903.
(10) Peden, C. H. Cu/Chabazite catalysts for 'Lean-Burn' vehicle emission control. *J. Catal.* **2019**, *373*, 384−389.
(11) Vennestrøm, P. N.; Thøgersen, J. R.; Gabrielsson, P. L.; Van Tendeloo, L.; Schütze, F.-W.; Moliner, M. Advances and perspectives from a decade of collaborative efforts on zeolites for selective catalytic reduction of NOx. *Microporous Mesoporous Mater.* **2023**, *358*, 112336.
(12) Moreno-González, M.; Millán, R.; Concepción, P.; Blasco, T.; Boronat, M. Spectroscopic Evidence and Density Functional Theory (DFT) Analysis of Low-Temperature Oxidation of Cu + to Cu 2+ NO x in Cu-CHA Catalysts: Implications for the SCR-NO x Reaction Mechanism. *ACS Catal.* **2019**, *9*, 2725−2738.
(13) Chen, L.; Janssens, T. V.; Vennestrøm, P. N.; Jansson, J.; Skoglundh, M.; Grönbeck, H. A Complete Multisite Reaction Mechanism for Low-Temperature NH3-SCR over Cu-CHA. *ACS Catal.* **2020**, *10*, 5646−5656.
(14) Borfecchia, E.; Beato, P.; Svelle, S.; Olsbye, U.; Lamberti, C.; Bordiga, S. Cu-CHA − a model system for applied selective redox catalysis. *Chem. Soc. Rev.* **2018**, *47*, 8097−8133.
(15) Signorile, M.; Borfecchia, E.; Bordiga, S.; Berlier, G. Influence of ion mobility on the redox and catalytic properties of Cu ions in zeolites. *Chemical Science* **2022**, *13*, 10238−10250.
(16) Nasello, N. D.; Usberti, N.; Iacobone, U.; Gramigni, F.; Hu, W.; Liu, S.; Nova, I.; Gao, X.; Tronconi, E.; Dual-Site, R. H. C.; Transient, O. H. C. Dual-Site RHC and OHC Transient Kinetics Predict Low-T Standard SCR Steady-State Rates over a Cu-CHA Catalyst. *ACS Catal.* **2023**, *13*, 2723−2734.
(17) Millan, R.; Cnudde, P.; Hoffman, A. E.; Lopes, C. W.; Concepción, P.; Van Speybroeck, V.; Boronat, M. Theoretical and Spectroscopic Evidence of the Dynamic Nature of Copper Active Sites in Cu-CHA Catalysts under Selective Catalytic Reduction (NH3-SCR-NOx) Conditions. *J. Phys. Chem. Lett.* **2020**, *11*, 10060−10066.
(18) Millan, R.; Cnudde, P.; Speybroeck, V. v.; Boronat, M. Mobility and Reactivity of Cu+ Species in Cu-CHA Catalysts under NH3-SCR-NOx Reaction Conditions: Insights from AIMD Simulations. *JACS Au* **2021**, *1*, 1778−1787.
(19) Martini, A.; Negri, C.; Bugarin, L.; Deplano, G.; Abasabadi, R. K.; Lomachenko, K. A.; Janssens, T. V.; Bordiga, S.; Berlier, G.; Borfecchia, E. Assessing the Influence of Zeolite Composition on Oxygen-Bridged Diamino Dicopper(II) Complexes in Cu-CHA DeNOxCatalysts by Machine Learning-Assisted X-ray Absorption Spectroscopy. *J. Phys. Chem. Lett.* **2022**, *13*, 6164−6170.
(20) Krishna, S. H.; Goswami, A.; Wang, Y.; Jones, C. B.; Dean, D. P.; Miller, J. T.; Schneider, W. F.; Gounder, R. Influence of framework Al density in chabazite zeolites on copper ion mobility and reactivity during NOx selective catalytic reduction with NH3. *Nature Catalysis 2023 6:3* **2023**, *6*, 276−285.
(21) Marberger, A.; Petrov, A. W.; Steiger, P.; Elsener, M.; Kröcher, O.; Nachtegaal, M.; Ferri, D. Time-resolved copper speciation during selective catalytic reduction of NO on Cu-SSZ-13. *Nature Catalysis 2018 1:3* **2018**, *1*, 221−227.
(22) Becher, J.; Sanchez, D. F.; Doronkin, D. E.; Zengel, D.; Meira, D. M.; Pascarelli, S.; Grunwaldt, J.-D.; Sheppard, T. L. Chemical gradients in automotive Cu-SSZ-13 catalysts for NOx removal revealed by operando X-ray spectrotomography. *Nat. Catal.* **2021**, *4*, 46−53.
(23) Wu, Y.; Zhao, W.; Ahn, S. H.; Wang, Y.; Walter, E. D.; Chen, Y.; Derewinski, M. A.; Washton, N. M.; Rappé, K. G.; Wang, Y.; Mei, D.; Hong, S. B.; Gao, F. Interplay between copper redox and transfer and support acidity and topology in low temperature NH3-SCR. *Nat. Commun.* **2023**, *14*, 2633.
(24) Van Speybroeck, V. Challenges in modelling dynamic processes in realistic nanostructured materials at operating conditions. *Philos. Trans. R. Soc. A* **2023**, *381*, 20220239.
(25) Fu, X.; Wu, Z.; Wang, W.; Xie, T.; Keten, S.; Gomez-Bombarelli, R.; Jaakkola, T. Forces are not Enough: Benchmark and Critical Evaluation for Machine Learning Force Fields with Molecular Simulations. 2022; preprint, https://arxiv.org/abs/2210.07237v1.
(26) Axelrod, S.; Schwalbe-Koda, D.; Mohapatra, S.; Damewood, J.; Greenman, K. P.; Gómez-Bombarelli, R. Learning Matter: Materials Design with Machine Learning and Atomistic Simulations. *Accounts of Materials Research* **2022**, *3*, 343−357.
(27) Schmidt, J.; Marques, M. R. G.; Botti, S.; Marques, M. A. L. Recent advances and applications of machine learning in solid-state materials science. *npj Computational Materials* **2019**, *5*, 83.
(28) Ma, S.; Liu, Z.-P. Machine Learning for Atomic Simulation and Activity Prediction in Heterogeneous Catalysis: Current Status and Future. *ACS Catal.* **2020**, *10*, 13213−13226.
(29) Goldsmith, B. R.; Esterhuizen, J.; Liu, J.-X. X. J.; Bartel, C. J.; Sutton, C. Machine learning for heterogeneous catalyst design and discovery. *AIChE J.* **2018**, *64*, 2311−2323.
(30) Schlexer Lamoureux, P.; Winther, K. T.; Garrido Torres, J. A.; Streibel, V.; Zhao, M.; Bajdich, M.; Abild-Pedersen, F.; Bligaard, T. Machine Learning for Computational Heterogeneous Catalysis. *ChemCatChem.* **2019**, *11*, 3581−3601.
(31) Gu, G. H.; Noh, J.; Kim, S.; Back, S.; Ulissi, Z.; Jung, Y. Practical Deep-Learning Representation for Fast Heterogeneous Catalyst Screening. *J. Phys. Chem. Lett.* **2020**, *11*, 3185−3191.
(32) Behler, J. Neural network potential-energy surfaces in chemistry: a tool for large-scale simulations. *Phys. Chem. Chem. Phys.* **2011**, *13*, 17930.
(33) Behler, J. First Principles Neural Network Potentials for Reactive Simulations of Large Molecular and Condensed Systems. *Angew. Chem., Int. Ed.* **2017**, *56*, 12828−12840.
(34) Botu, V.; Batra, R.; Chapman, J.; Ramprasad, R. Machine learning force fields: Construction, validation, and outlook. *J. Phys. Chem. C* **2017**, *121*, 511−522.
(35) Mueller, T.; Hernandez, A.; Wang, C. Machine learning for interatomic potential models. *J. Chem. Phys.* **2020**, *152*, 50902.
(36) von Lilienfeld, O. A.; Müller, K.-R. R.; Tkatchenko, A. Exploring chemical compound space with quantum-based machine learning. *Nature Reviews Chemistry* **2020**, *4*, 347−358.
(37) Noé, F.; Olsson, S.; Köhler, J.; Wu, H. Boltzmann generators: Sampling equilibrium states of many-body systems with deep learning. *Science* **2019**, *365*, eaaw1147.
(38) Coley, C. W.; Eyke, N. S.; Jensen, K. F. Autonomous discovery in the chemical sciences part I: Progress. *Angew. Chem., Int. Ed.* **2020**, *59*, 22858−22893.
(39) Butler, K. T.; Davies, D. W.; Cartwright, H.; Isayev, O.; Walsh, A. Machine learning for molecular and materials science. *Nature* **2018**, *559*, 547−555.

https://doi.org/10.1021/acscentsci.3c00870
ACS Cent. Sci. 2023, 9, 2044−2056

(40) Erlebach, A.; Nachtigall, P.; Grajciar, L. Accurate large-scale simulations of siliceous zeolites by neural network potentials. *npj Computational Materials 2022 8:1* **2022**, *8*, 174.
(41) Moliner, M.; Román-Leshkov, Y.; Corma, A. Machine Learning Applied to Zeolite Synthesis: The Missing Link for Realizing High-Throughput Discovery. *Acc. Chem. Res.* **2019**, *52*, 2971−2980.
(42) Chmiela, S.; Sauceda, H. E.; Müller, K.-R.; Tkatchenko, A. Towards exact molecular dynamics simulations with machine-learned force fields. *Nat. Commun.* **2018**, *9*, 3887.
(43) Sosso, G. C.; Miceli, G.; Caravati, S.; Behler, J.; Bernasconi, M. Neural network interatomic potential for the phase change material GeTe. *Phys. Rev. B* **2012**, *85*, 174103.
(44) Bernstein, N.; Bhattarai, B.; Csunyi, G.; Drabold, D. A.; Elliott, S. R.; Deringer, V. L.; Bernstein, N.; Bhattarai, B.; Drabold, R. D. A.; Csunyi, G.; Deringer, V. L.; Elliott, S. R. Quantifying Chemical Structure and Machine-Learned Atomic Energies in Amorphous and Liquid Silicon. *Angew. Chem., Int. Ed.* **2019**, *58*, 7057−7061.
(45) Smith, J. S.; Isayev, O.; Roitberg, A. E. ANI-1, A data set of 20 million calculated off-equilibrium conformations for organic molecules. *Scientific Data* **2017**, *4*, 170193.
(46) Smith, J. S.; Isayev, O.; Roitberg, A. E. ANI-1: an extensible neural network potential with DFT accuracy at force field computational cost. *Chemical Science* **2017**, *8*, 3192−3203.
(47) Smith, J. S.; Nebgen, B. T.; Zubatyuk, R.; Lubbers, N.; Devereux, C.; Barros, K.; Tretiak, S.; Isayev, O.; Roitberg, A. E. Approaching coupled cluster accuracy with a general-purpose neural network potential through transfer learning. *Nat. Commun.* **2019**, *10*, 2903.
(48) Devereux, C.; Smith, J. S.; Huddleston, K. K.; Barros, K.; Zubatyuk, R.; Isayev, O.; Roitberg, A. E. Extending the Applicability of the ANI Deep Learning Molecular Potential to Sulfur and Halogens. *J. Chem. Theory Comput.* **2020**, *16*, 4192−4202.
(49) Schütt, K. T.; Arbabzadah, F.; Chmiela, S.; Müller, K. R.; Tkatchenko, A. Quantum-chemical insights from deep tensor neural networks. *Nat. Commun.* **2017**, *8*, 13890.
(50) Schütt, K. T.; Kessel, P.; Gastegger, M.; Nicoli, K. A.; Tkatchenko, A.; Müller, K. R. SchNetPack: ADeep Learning Toolbox for Atomistic Systems. *J. Chem. Theory Comput.* **2019**, *15*, 448−455.
(51) Zhang, L.; Han, J.; Wang, H.; Car, R.; Weinan, E. Deep Potential Molecular Dynamics: A Scalable Model with the Accuracy of Quantum Mechanics. *Phys. Rev. Lett.* **2018**, *120*, 143001.
(52) Chen, C.; Ye, W.; Zuo, Y.; Zheng, C.; Ong, S. P. Graph Networks as a Universal Machine Learning Framework for Molecules and Crystals. *Chem. Mater.* **2019**, *31*, 3564−3572.
(53) Klicpera, J.; Groß, J.; Günnemann, S. Directional message passing for molecular graphs. *ICLR* 2020; pp 1−13.
(54) Qiao, Z.; Welborn, M.; Anandkumar, A.; Manby, F. R.; Miller, T. F. OrbNet: Deep learning for quantum chemistry using symmetry-adapted atomic-orbital features. *J. Chem. Phys.* **2020**, *153*, 124111.
(55) Schütt, K. T.; Unke, O. T.; Gastegger, M. Equivariant message passing for the prediction of tensorial properties and molecular spectra. 2021; preprint, https://arxiv.org/abs/2102.03150.
(56) Batzner, S.; Musaelian, A.; Sun, L.; Geiger, M.; Mailoa, J. P.; Kornbluth, M.; Molinari, N.; Smidt, T. E.; Kozinsky, B. E(3)-Equivariant Graph Neural Networks for Data-Efficient and Accurate Interatomic Potentials. *Nat. Commun.* **2022**, *13*, 2453.
(57) Artrith, N.; Urban, A. An implementation of artificial neural-network potentials for atomistic materials simulations: Performance for TiO2. *Comput. Mater. Sci.* **2016**, *114*, 135−150.
(58) Vandenhaute, S.; Cools-Ceuppens, M.; DeKeyser, S.; Verstraelen, T.; Van Speybroeck, V. Machine learning potentials for metal-organic frameworks using an incremental learning approach. *npj Computational Materials* **2023**, *9*, 19.
(59) Bocus, M.; Goeminne, R.; Lamaire, A.; Cools-Ceuppens, M.; Verstraelen, T.; Van Speybroeck, V. Nuclear quantum effects on zeolite proton hopping kinetics explored with machine learning potentials and path integral molecular dynamics. *Nat. Commun.* **2023**, *14*, 1008.
(60) Winter, G.; Gómez-Bombarelli, R. Simulations with machine learning potentials identify the ion conduction mechanism mediating non-Arrhenius behavior in LGPS. 2022; preprint, http://arxiv.org/abs/2211.05713v2.
(61) Gastegger, M.; Marquetand, P. High-Dimensional Neural Network Potentials for Organic Reactions and an Improved Training Algorithm. *J. Chem. Theory Comput.* **2015**, *11*, 2187−2198.
(62) Ang, S. J.; Wang, W.; Schwalbe-Koda, D.; Axelrod, S.; Gómez-Bombarelli, R. Active learning accelerates ab initio molecular dynamics on reactive energy surfaces. *Chem.* **2021**, *7*, 738−751.
(63) Du, X.; Damewood, J. K.; Lunger, J. R.; Millan, R.; Yildiz, B.; Li, L.; Gómez-Bombarelli, R. Machine-learning-accelerated simulations enable heuristic-free surface reconstruction. 2023; preprint, https://arxiv.org/abs/2305.07251.
(64) Erlebach, A.; Nachtigall, P.; Grajciar, L. Accurate large-scale simulations of siliceous zeolites by neural network potentials. *NPJ Comput. Mater.* **2022**, 174.
(65) Ma, S.; Liu, Z.-P. Machine learning potential era of zeolite simulation. *Chem. Sci.* **2022**, *13*, 5055−5068.
(66) Behler, J. Constructing high-dimensional neural network potentials: A tutorial review. *Int. J. Quantum Chem.* **2015**, *115*, 1032−1050.
(67) Smith, J. S.; Nebgen, B.; Lubbers, N.; Isayev, O.; Roitberg, A. E. Less is more: Sampling chemical space with active learning. *J. Chem. Phys.* **2018**, *148*, 241733.
(68) Schran, C.; Brezina, K.; Marsalek, O. Committee neural network potentials control generalization errors and enable active learning. *J. Chem. Phys.* **2020**, *153*, 104105.
(69) Musil, F.; Willatt, M. J.; Langovoy, M. A.; Ceriotti, M. Fast and Accurate Uncertainty Estimation in Chemical Machine Learning. *J. Chem. Theory Comput.* **2019**, *15*, 906−915.
(70) Peterson, A. A.; Christensen, R.; Khorshidi, A. Addressing uncertainty in atomistic machine learning. *Phys. Chem. Chem. Phys.* **2017**, *19*, 10978−10985.
(71) Lookman, T.; Balachandran, P. V.; Xue, D.; Yuan, R. Active learning in materials science with emphasis on adaptive sampling using uncertainties for targeted design. *npj Computational Materials* **2019**, *5*, 21.
(72) Shapeev, A.; Gubaev, K.; Tsymbalov, E.; Podryabinkin, E. In *Machine Learning Meets Quantum Physics*; Schütt, K. T., Chmiela, S., von Lilienfeld, O. A., Tkatchenko, A., Tsuda, K., Müller, K.-R., Eds.; Springer International Publishing: Cham, 2020; pp 309−329.
(73) Imbalzano, G.; Zhuang, Y.; Kapil, V.; Rossi, K.; Engel, E. A.; Grasselli, F.; Ceriotti, M. Uncertainty estimation for molecular dynamics and sampling. *J. Chem. Phys.* **2021**, *154*, 74102.
(74) Wang, W.; Yang, T.; Harris, W. H.; Gómez-Bombarelli, R. Active learning and neural network potentials accelerate molecular screening of ether-based solvate ionic liquids. *Chem. Commun.* **2020**, *56*, 8920−8923.
(75) Schwalbe-Koda, D.; Tan, A. R.; Gómez-Bombarelli, R. Differentiable sampling of molecular geometries with uncertainty-based adversarial attacks. *Nat. Commun.* **2021**, *12*, 5104.
(76) Wang, W.; Axelrod, S.; Gómez-Bombarelli, R. Differentiable Molecular Simulations for Control and Learning. 2020; preprint, http://arxiv.org/abs/2003.00868.
(77) Tan, A. R.; Urata, S.; Goldman, S.; Dietschreit, J. C. B.; Gómez-Bombarelli, R. Single-model uncertainty quantification in neural network potentials does not consistently outperform model ensembles. 2023; preprint, https://arxiv.org/abs/2305.01754v1.
(78) McInnes, L.; Healy, J.; Saul, N.; Großberger, L. UMAP: Uniform Manifold Approximation and Projection. *Journal of Open Source Software* **2018**, *3*, 861.
(79) Xie, T.; Grossman, J. C. Crystal Graph Convolutional Neural Networks for an Accurate and Interpretable Prediction of Material Properties. *Phys. Rev. Lett.* **2018**, *120*, 145301.
(80) Shwan, S.; Skoglundh, M.; Lundegaard, L. F.; Tiruvalam, R. R.; Janssens, T. V.; Carlsson, A.; Vennestrøm, P. N. Solid-State Ion-Exchange of Copper into Zeolites Facilitated by Ammonia at Low Temperature. *ACS Catal.* **2015**, *5*, 16−19.

https://doi.org/10.1021/acscentsci.3c00870
ACS Cent. Sci. 2023, 9, 2044−2056

(81) Vennestrøm, P. N.; Lundegaard, L. F.; Tyrsted, C.; Bokarev, D. A.; Mytareva, A. I.; Baeva, G. N.; Stakheev, A. Y.; Janssens, T. V. The Role of Protons and Formation $Cu(NH_3)_2^+$ During Ammonia-Assisted Solid-State Ion Exchange of Copper(I) Oxide into Zeolites. *Top. Catal.* **2019**, *62*, 100−107.
(82) Sípka, M.; Dietschreit, J. C. B.; Grajciar, L.; Gómez-Bombarelli, R. Differentiable Simulations for Enhanced Sampling of Rare Events. 2023; preprint, https://arxiv.org/abs/2301.03480.

https://doi.org/10.1021/acscentsci.3c00870
ACS Cent. Sci. 2023, 9, 2044−2056